IJL, Vol. 25, Issue 1, 2026
http://doi.org/10.31900/ijl.v25i1.563

Research Article

Laser Direct Energy Deposition of Stainless Steel 316L: Investigation of Processing Parameters on Porosity and Microstructural Evolution

Samir Noori Ali[1,*], Ziad Aeyad Taha[1], Barbara Previtali[2]

[1]Institute of Laser for Postgraduate Studies, University of Baghdad, Baghdad, Iraq
[2]Department of Mechanical Engineering, Politecnico di Milano, Via La Masa 1, 20156 Milan, Italy
**Email address of the Corresponding author: samirnoori@ilps.uobaghdad.edu.iq*

Article history: Received 21 Jan. 2026, Accepted 6 Mar. 2026, Published online 15 Jun. 2026

Abstract: Laser direct energy deposition (LDED) was employed to fabricate low-carbon stainless steel 316L and to evaluate the influence of processing parameters on porosity, relative density, and microhardness. A fiber laser system operating at 1070 nm (YLS-3000-CUT, IPG ABB) was used. The spot size was 1.2 mm, the powder feed rate was 9.5 g/min, the layer thickness was 0.2 mm, the carrier gas flow rate was 7.5 L/min, and the shielding gas flow rate was 25 L/min. Laser power (420, 600, and 800 W) and scan speed (20, 25, and 30 mm/s) were systematically varied, producing nine samples with linear energy densities between 14 and 40 J/mm and volumetric energy densities from 59 to 167 J/mm^3. Microstructural features and pore morphology were examined using optical microscopy and scanning electron microscopy. Porosity and relative density were quantified by full cross-sectional image analysis. Microhardness was measured using a Vickers indenter with a 300 g load and 10 s dwell time. Microhardness values ranged from 185.4 to 207.3 HV. Porosity values varied between 0.198% and 0.831%, while relative density ranged from 99.169% to 99.802%. Lower volumetric energy densities produced reduced porosity and increased relative density at all scan speeds. The minimum porosity (0.198%) and maximum relative density (99.802%) were obtained at a scan speed of 30 mm/s and a volumetric energy density of 59 J/mm^3. The results quantify the effect of laser power and scan speed on densification and mechanical response in LDED-processed 316L and define a limited processing window for defect minimization.

Keywords: Laser direct energy deposition, Energy density, Scan speed.

1. Introduction

Laser direct energy deposition (LDED) is an additive manufacturing technique used to fabricate complex three-dimensional metallic components with reduced material waste and high deposition flexibility [1]. In LDED, metallic powder or wire feedstock is injected into a focused laser beam, where it melts and is deposited onto a substrate in a layer-by-layer manner [2]. This process enables near-net-shape manufacturing and repair of high-value components that are difficult or impractical to produce using conventional machining routes. Despite these advantages, the adoption of LDED for safety-critical applications remains limited due to the formation of process-induced defects, particularly porosity [3]. Porosity in LDED arises from multiple mechanisms, including gas entrapment within the melt pool, lack-of-fusion between adjacent tracks or layers, keyhole instability, and pre-existing pores in atomized powder feedstock [4]. Even at low volume fractions, such defects can significantly degrade mechanical performance, especially tensile strength, ductility, and fatigue resistance [5]. The severity of these effects depends strongly on pore morphology and spatial distribution. Irregular lack-of-fusion pores generally exert a more detrimental influence on mechanical properties than spherical gas pores of comparable size, highlighting the need to control both pore formation mechanisms and their evolution during deposition [6].

Austenitic stainless steel 316L is widely used in marine, chemical, and biomedical applications due to its corrosion resistance, moderate strength, and excellent weldability [7]. In LDED processing, material quality is strongly governed by energy input, commonly expressed as energy density. Laser power and scan speed directly regulate the thermal energy delivered per unit length, thereby influencing melt pool geometry, cooling rate, solidification behavior, and defect formation [8]. Insufficient energy input leads to incomplete fusion and lack-of-fusion porosity, whereas excessive energy input promotes keyhole formation and subsequent gas entrapment during collapse [9]. Achieving full densification therefore requires a balanced processing window that enables adequate fusion while minimizing excessive vaporization and instability [10].

Although prior studies have demonstrated the sensitivity of porosity to processing parameters, the combined and systematic effects of laser power and scan speed on porosity characteristics, microstructural evolution, relative density, and mechanical response remain insufficiently resolved, particularly for 316L fabricated by LDED [11]. In addition, many investigations report microstructural observations without directly linking them to quantified porosity levels and local mechanical properties. This limits the ability to establish reliable process–structure–property relationships.

Microstructural characterization using optical microscopy and scanning electron microscopy provides essential insight into grain morphology, dendritic structure, phase distribution, and defect types formed during LDED [12]. Complementary microhardness measurements serve as a sensitive indicator of local microstructural variations and compositional inhomogeneity induced by thermal history. Together, these techniques enable correlation between processing conditions, microstructural features, and mechanical response at the microscale. Such correlations are necessary for defining processing windows suitable for defect minimization and performance consistency [13].

Several recent studies highlight both the potential and limitations of DED-based processing of stainless steels. Saboori et al. [14] emphasized that although DED enables fabrication of complex and functionally graded structures, incomplete understanding of microstructure evolution and defect formation continues to hinder industrial maturity. G. A. Barragán et al. [15] demonstrated that directed energy deposition (DED) can produce dense AISI 316L stainless steel deposits with strong metallurgical bonding and low porosity when appropriate processing conditions are employed. Their results confirmed that high cooling rates inherent to DED promote fine cellular and dendritic austenitic microstructures, which are closely associated with improved material integrity. Although their study focused on coating applications, it highlighted the importance of controlling process parameters to minimize porosity and preserve alloy chemistry during deposition.

H. Shi et al. [16] investigated the influence of additive manufacturing–induced microstructural features on the high-temperature behavior of laser metal deposited 316L stainless steel. Their work showed that phase segregation and δ-ferrite formation at grain boundaries are strongly linked to thermal history and energy input during deposition. These findings emphasize that process-controlled microstructural evolution plays a critical role in determining material performance, reinforcing the need for systematic parameter control in LDED. Zhou and Ning et al. [17] examined the effects of process parameters on porosity formation and microstructural refinement in DED-fabricated 316L-based systems. Their study demonstrated that variations in energy input significantly affect melt pool stability, grain morphology, and defect formation.

Increased energy density promoted grain refinement but also increased the likelihood of porosity and cracking when excessive thermal input led to melt pool instability. This highlights the narrow processing window required to balance densification and defect suppression.

Z. Ma et al. [18] reported that multiple DED process parameters simultaneously influence density, surface quality, and microstructural uniformity in stainless steel–based structures. Their statistical analysis showed that scan speed plays a dominant role in controlling surface integrity, while thermal input strongly affects densification behavior. These results underscore the necessity of isolating and quantifying the individual and combined effects of laser power and scan speed on relative density and defect formation.

Zürcher et al. [19] investigated the wear behavior of additively manufactured 316L stainless steel produced by the laser metal deposition (LMD) process, with a specific focus on its suitability for repair applications. The authors evaluated friction and wear under dry sliding conditions using a flat-on-flat configuration against AISI 52100 steel and compared LMD-fabricated 316L with conventionally rolled 316L. Microstructure, residual stresses, and hardness were characterized prior to tribological testing to support interpretation of wear mechanisms.

Despite these advances, a quantitative and systematic correlation between laser power, scan speed, porosity, relative density, microstructural characteristics, and microhardness in LDED-fabricated 316L stainless steel remains limited [20]. Experimental studies that directly link energy density regimes to both defect metrics and mechanical response under controlled conditions are scarce [21].

Accordingly, the present work focuses on systematically varying laser power and scan speed during LDED of 316L stainless steel to quantify their effects on porosity formation, relative density, microstructure, and microhardness. By combining optical microscopy, scanning electron microscopy, image-based porosity analysis, and microhardness testing, this study establishes evidence-based process–structure–property relationships consistent with the scope defined in the abstract.

2. Materials and Methods

This section outlines the materials used, the experimental setup employed for laser direct energy deposition, and the processing parameters selected to fabricate 316L stainless steel samples. It also describes the characterization techniques applied to evaluate the microstructural, mechanical, and porosity-related features of the deposited materials, along with the methodology used to quantify porosity and assess the quality of the fabricated parts.

2.1. Materials

Low-carbon austenitic stainless steel 316L powder was used as the feedstock material for laser direct energy deposition. The powder particle size ranged from 56 to 100 μm, which was made by the gas atomization manufacturing method, ensuring stable flowability and consistent interaction with the laser-induced melt pool, as shown in Fig. 1. Also, the volumetric distribution and volume transformation are shown in Figs. 2and 3 respectively. The chemical composition of SS316L powder was summarized in Table 1.

Table 1. Chemical composition of SS316L (Wt.%)

Fe%	C%	Cr%	Mn%	Mo%	P%	Si%	Ni%
Bal.	0.03	19.09	1.14	2.32	0.5	0.71	10.07

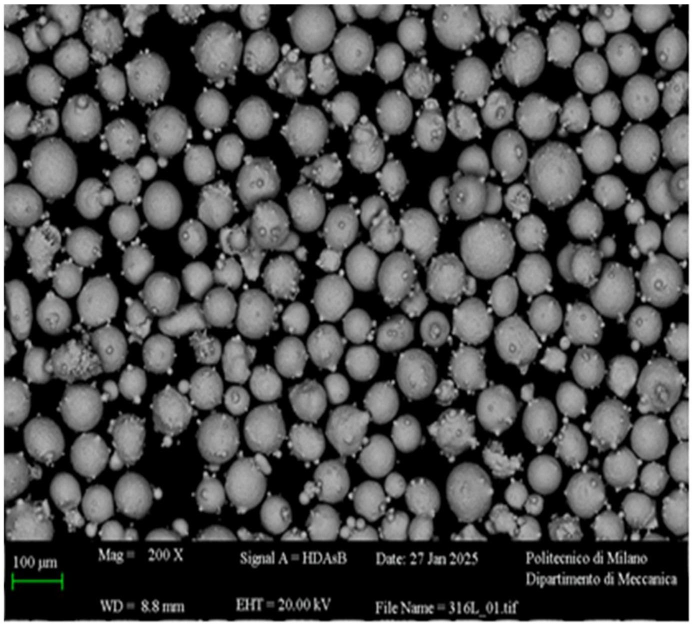

Fig. 1: SEM of SS316L powder

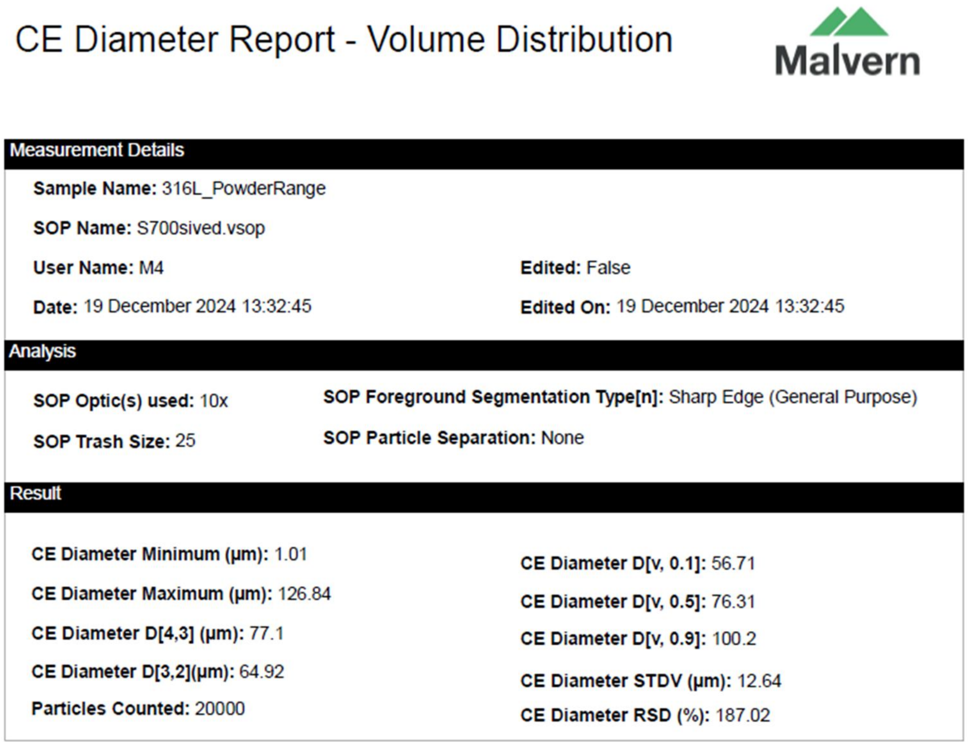

CE Diameter Report - Volume Distribution

Malvern

Measurement Details

Sample Name: 316L_PowderRange
SOP Name: S700sived.vsop
User Name: M4
Edited: False
Date: 19 December 2024 13:32:45
Edited On: 19 December 2024 13:32:45

Analysis

SOP Optic(s) used: 10x
SOP Foreground Segmentation Type[n]: Sharp Edge (General Purpose)
SOP Trash Size: 25
SOP Particle Separation: None

Result

CE Diameter Minimum (µm): 1.01
CE Diameter Maximum (µm): 126.84
CE Diameter D[4,3] (µm): 77.1
CE Diameter D[3,2](µm): 64.92
Particles Counted: 20000
CE Diameter D[v, 0.1]: 56.71
CE Diameter D[v, 0.5]: 76.31
CE Diameter D[v, 0.9]: 100.2
CE Diameter STDV (µm): 12.64
CE Diameter RSD (%): 187.02

Fig. 2: Volume distribution of SS316L

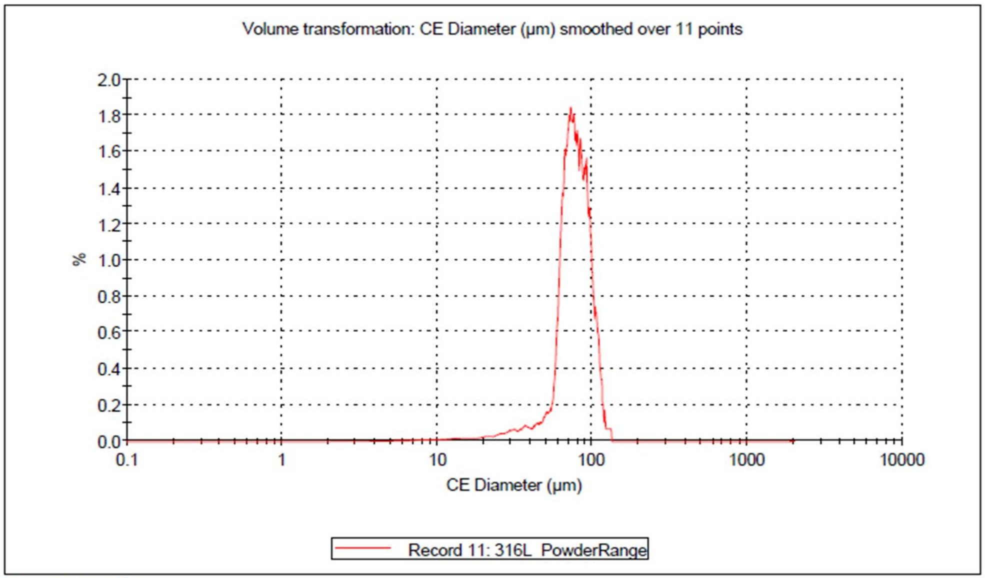

Comments: 10x
13mm

Fig. 3: Volume transformation of SS316L.

2.2 Experimental Setup

The laser direct energy deposition (LDED) process was carried out using a high-power fiber laser system (YLS-3000-CUT, IPG ABB) operating at a wavelength of 1070 nm with a Gaussian beam intensity distribution, as shown in *Fig. 4*. The system was integrated with an ABB industrial robotic arm coupled with a circular two-axis table, enabling precise multi-axis motion control and flexible deposition strategies. A coaxial powder delivery system transported SS316L powder from a hopper to the laser focal point using argon carrier gas at 7.5 L/min, while argon shielding gas at 25 L/min was supplied around the melt pool to minimize oxidation and atmospheric contamination during deposition.

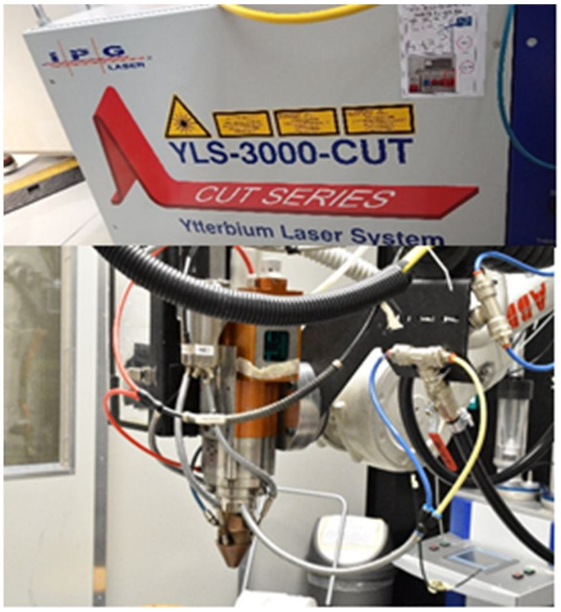

Fig. 4: Ytterbium fiber laser and LDED printhead.

2.3. Process Parameters

A fixed laser spot size of 1.2 mm, layer thickness of 0.2 mm, powder feed rate of 9.5 g/min, overlap of 50%, and hatch spacing of 0.6 mm, which is typical for LDED processes and ensures sufficient melt pool overlap for good metallurgical bonding, while limiting excessive reheating, and standoff distance of 12 mm. All these characteristics were maintained throughout the experiments. The process parameters were systematically varied by adjusting laser power (420, 600, and 800 W) and scan speed (20, 25, and 30 mm/s), resulting in nine distinct deposition conditions. These parameter combinations produced linear energy densities ranging from 14 J/mm to 40 J/mm, allowing investigation of their influence on melt pool behavior, thermal gradients, solidification dynamics, and resulting microstructural and mechanical properties.

The basic relationship of material quality in LDED is the volumetric energy density (VED) in J/mm³, mathematically expressed as [22].

$$VED = \frac{P}{v\,t\,d} \qquad (1)$$

where P laser power (W), v scan speed (mm/s), d spot diameter (mm), and t layer thickness (mm).

Nevertheless, for single-track depositions, the fixed spot size (1.2 mm) and layer thickness (0.2 mm) in each deposition track, the linear energy density, mathematically specified as [22],becomes the dominant parameter controlling melt pool characteristics.

$$El = \frac{P}{v} \qquad (2)$$

2.4. Characterization Methods

The deposited samples, each with dimensions of 10 x 10 x 10 mm³, as shown in *Fig. 5*, were built by zigzag for cubes strategy. All samples were sectioned, mounted, polished, and prepared following standard metallographic procedures, as shown in Fig. 6. The metallographically prepared samples were chemically etched using an aqueous solution composed of hydrochloric acid (HCl), nitric acid (HNO_3), and distilled water mixed in a 1:1:1 volume ratio to reveal the microstructural features [23].

Optical microscopy (OM) and scanning electron microscopy (SEM) were employed to analyze microstructural features, grain morphology, phase distribution, and defect characteristics. To evaluate mechanical behavior, Vickers microhardness testing was performed using a load of 300 g and a dwell time of 10 s, enabling assessment of local property variations caused by microstructural evolution and porosity distribution, as shown in Fig. 7[24,25].
Hardness profiles were obtained along three vertical traverses across the cross-section (edge–center–edge) from the substrate interface to the top of the deposited height. A total of 150 independent indentations were conducted, consisting of 50 measurements along each traverse. A minimum center-to-center spacing of at least three times the indentation diagonal length was maintained between adjacent indents to avoid interaction effects, in accordance with ASTM E384. The hardness values obtained from each traverse were subsequently averaged, and the mean values were used for plotting and comparative analysis, as shown in Fig. 8.

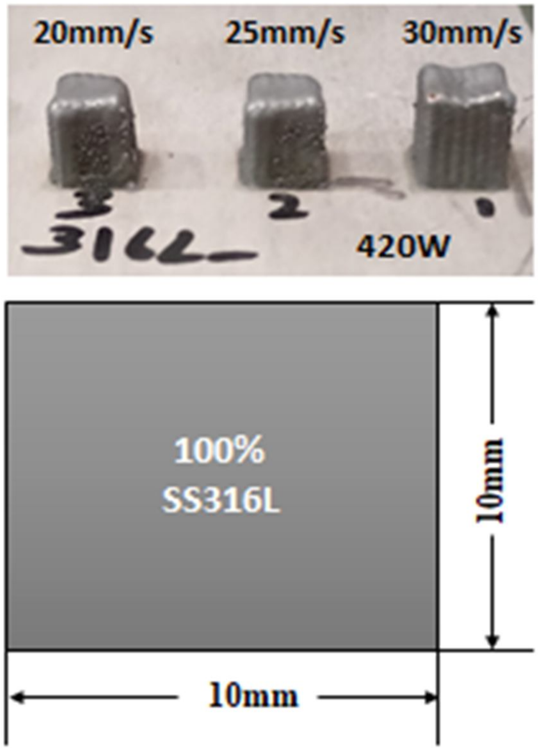

Fig. 5: dimensions of SS316L samples.

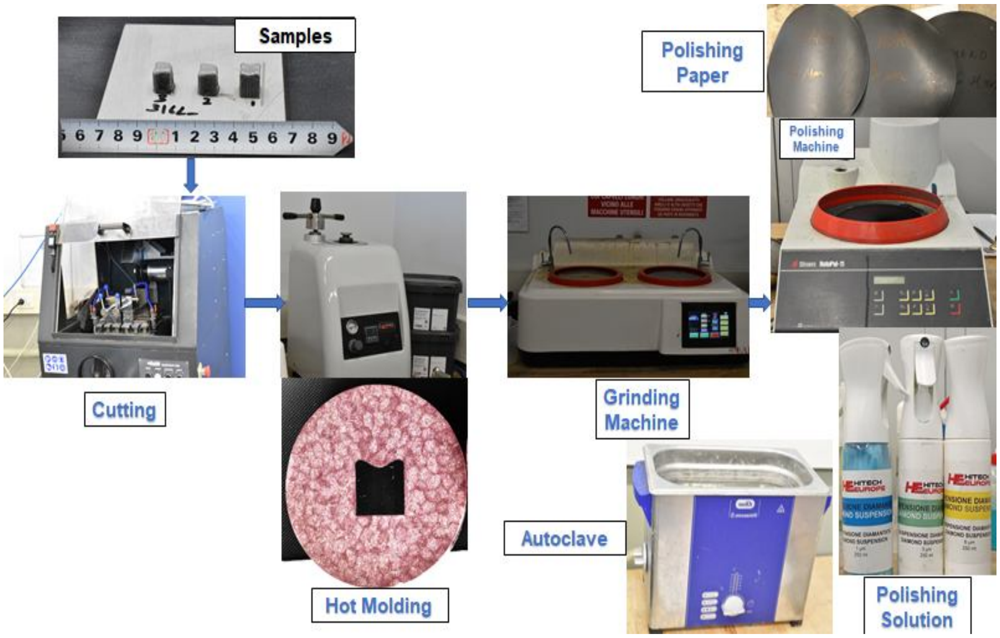

Fig. 6: Sample preparation procedure.

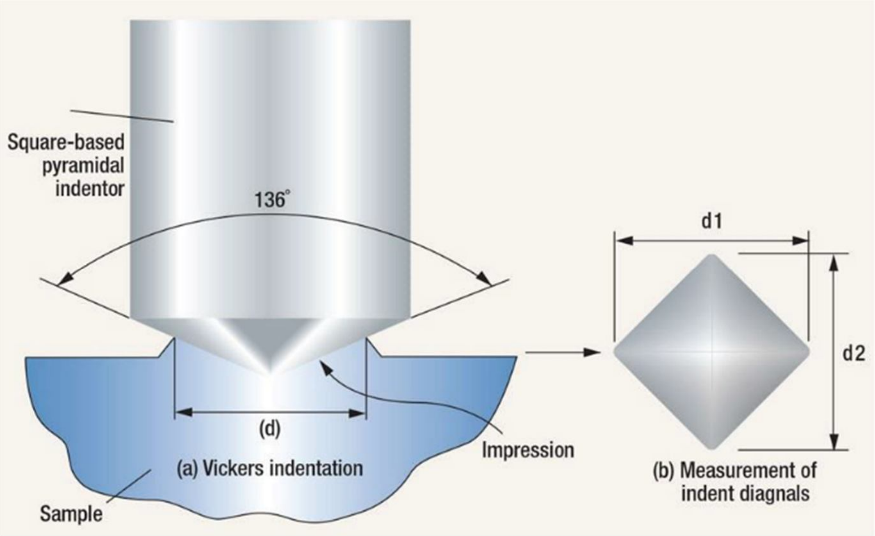

Fig. 7: Principal of Hardness Vickers Calculation [24].

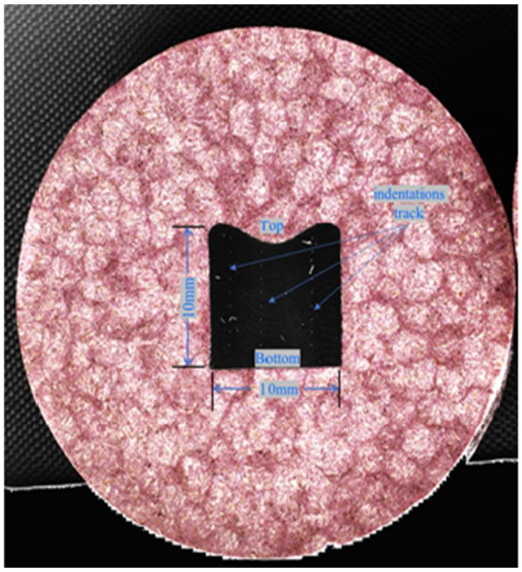

Fig. 8: Microhardness profiles measured along the build height of SS316L.

2.5. Porosity Quantification Methodology

Porosity and relative density were quantified using high-resolution optical images captured across the full cross-sectional area of each specimen with a Mitutoyo Quick Vision optical measurement system. Quantitative porosity analysis was performed using ImageJ software. Optical micrographs acquired from polished and etched cross-sections were used for analysis. For each sample, multiple images were captured at identical magnification from representative regions across the deposited area to ensure statistical reliability. The images were first converted to grayscale and subjected to contrast enhancement to improve pore–matrix differentiation. A global thresholding method was applied to segment pores from the metallic matrix, followed by manual verification to remove artifacts and non-relevant features.

Porosity was quantified by calculating the ratio of the total pore area to the total analyzed area. The reported porosity values represent the average of all analyzed images for each processing condition.

3. Results and discussion

3.1. Porosity and Relative Density

At the lab, the experimental results showed that the linear energy density controls are essential to the optimum densification and the lowest porosity of laser-directed energy deposited samples. Importantly, we report that samples fabricated at the lowest energy densities (such as 420 W and higher scan speeds of 25 and 30 mm/s) resulted in the highest comparative density and least porosity, demonstrating stable melt pool dynamics, complete powder fusion, and suppressed overheating-induced defects. The thermal energy overabundance on samples had negatively impacted the porosity of different melt parameters [26], as such, we compared the results with those produced under high energy densities (higher power, lower scan-speed values), confirming that the increase of thermal energy caused the melt pool to destabilize, with attendant pore formation through keyhole instability and other mechanisms. Accordingly, this experiment proves from a systemic perspective that exact moderation of energy input is vital, and that the best structural, mechanical properties and build quality can only be obtained if the lowest linear energy densities are applied to the parameter matrix under consideration.

Analysis of the nine samples (see Figs. 9 and 10) reveals a strong relationship between linear energy density and porosity and the relative density of the laser-deposited structures. The samples have the lowest porosity and highest relative density at minimized energy densities using lower laser power and increased scan speed, indicating that the melt pool stability and efficient fusion without causing the melt to overheat. For instance, the sample processed at 420 W and 30 mm/s yielded the lowest porosity (0.198%) and the highest relative density (99.802%).

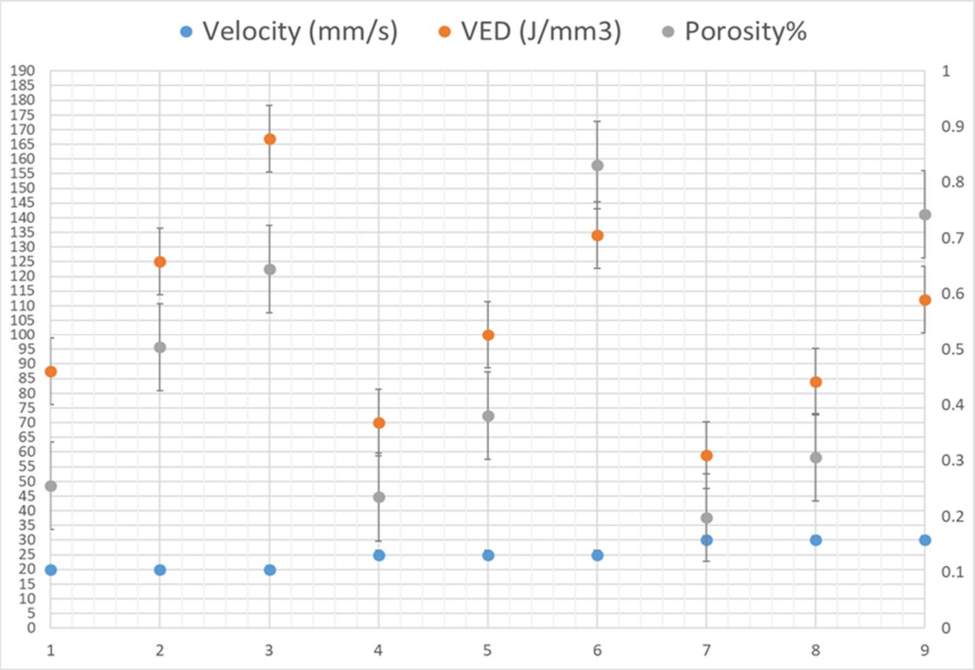

Fig. 9: Relationship between ν, VED, and porosity

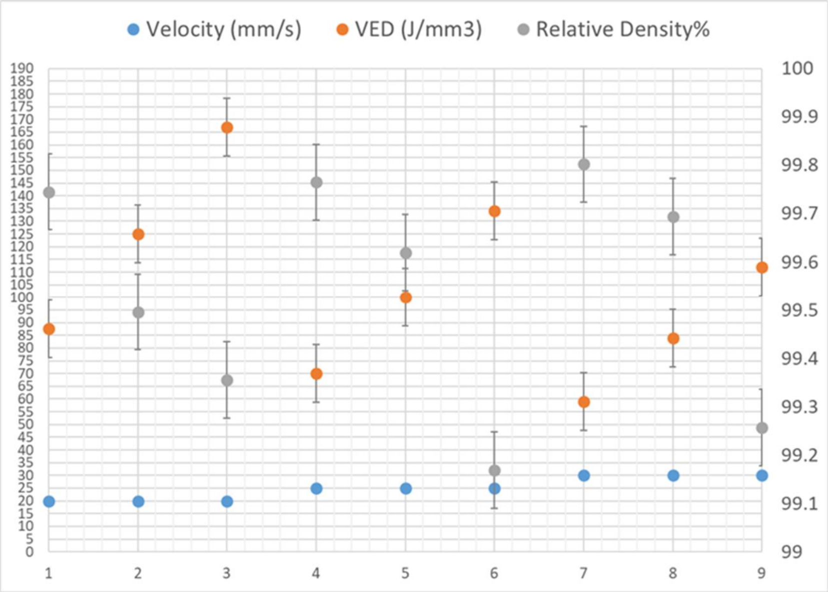

Fig. 10: Relationship between v, VED, and RD.

3.2. Microstructure Analysis

The microstructural evolution observed by OM and SEM can be understood as a continuous response to increasing energy per unit length (E_l) and the attendant changes in melt-pool geometry and local cooling rate: the lowest E_l runs (420 W at 30 mm/s, $E_l \approx 14$ J/mm as shown in Fig. 11) produce narrow, shallow, regularly stacked melt pools with only tiny, isolated spherical pores visible in OM and, in SEM, the finest cellular solidification substructure with extremely primary spacings, minimal interdendritic segregation, and only sparse, discontinuous carbide/oxide inclusions.

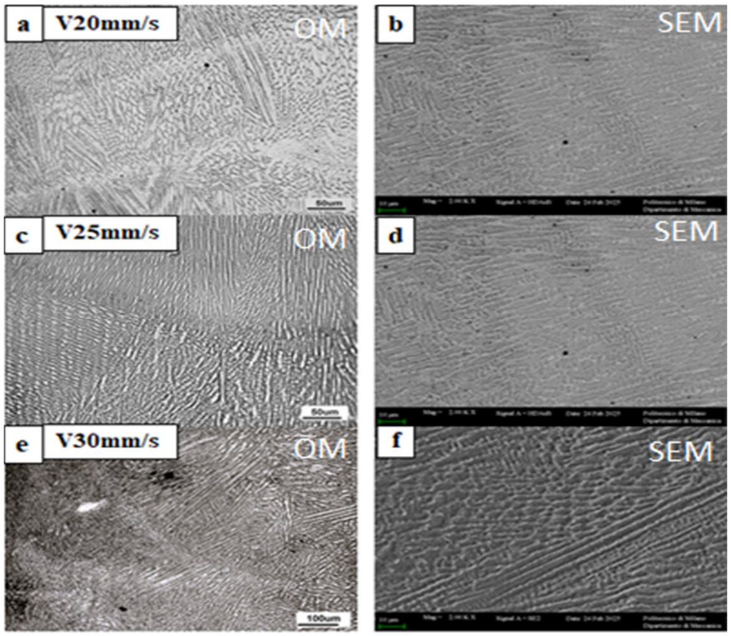

Fig. 11: OM and SEM of SS316L, v of 20, 25, and 30 mm/s at a P of 420 W

Considerably higher E_l at 420 W (Fig. 11) but slower speeds (25 mm/s and 20 mm/s; $E_l \approx 16.8$ and 21 J/mm) still show well-defined melt-pool bands in OM but progressively wider pools and a small increase in visible pore frequency, while SEM reveals a modest coarsening of cellular/dendritic spacing and a slightly greater tendency for solute and inclusion accumulation at cell walls.

Increasing power to 600 W (Fig. 12) at 30, 25, and 20 mm/s ($E_l \approx 20$, 24, and 30 J/mm) produces wider and deeper melt pools with more frequent small porosity and more irregular overlap footprints in OM; at the SEM scale these conditions exhibit coarser cellular/dendritic arrays, clearer enrichment of alloying elements and inclusion/precipitate contrast at interdendritic locations (manifested in SS316L as more pronounced cell-wall segregation and a likely presence of fine M23C6-type carbide or oxide clustering at boundaries), and a higher incidence of irregular porosity associated with partial keyholing or entrapment during slower solidification [27,28].

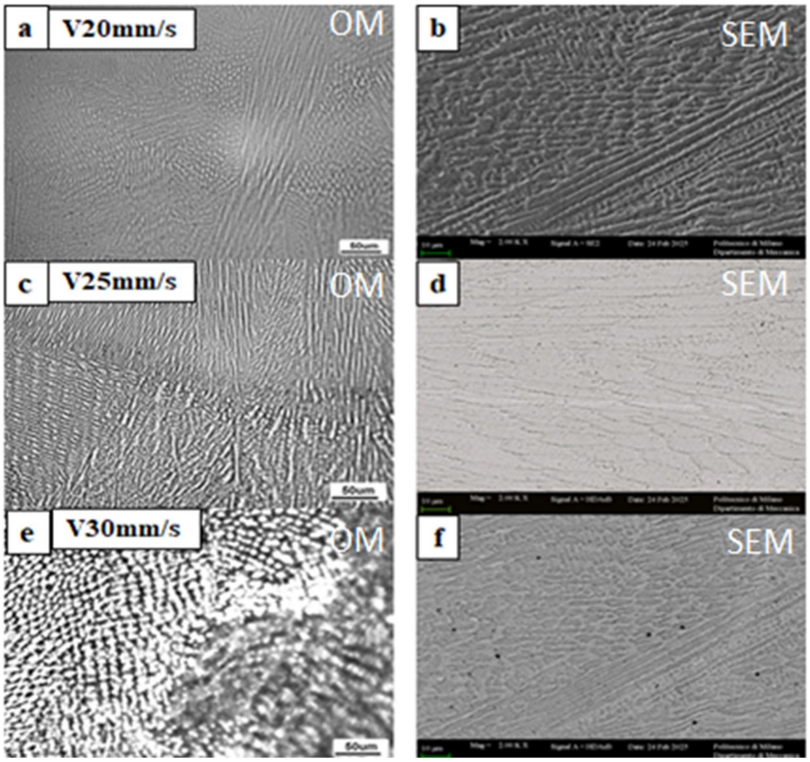

Fig. 12: OM and SEM of SS316L, ν of 20, 25, and 30 mm/s at a P of 600 W

At the highest power, 800 W (Fig. 13) with the three speeds ($E_l \approx 27$, 32, and 40 J/mm), OM shows the broadest, deepest, and most irregular melt pools with the greatest density of both spherical and irregular voids and disturbed overlaps, while SEM reveals markedly coarsened dendritic structures, extensive interdendritic films of segregated solute, and larger inclusion/precipitate particles and networks at grain boundaries; these microstructural features reflect long liquid lifetimes that enable solute partitioning, carbide/oxide precipitation, and coarsening and increase the probability of gas/vapor-induced porosity and lack-of-fusion defects from keyholing [29,30].

As shown in Figs. 11, 12 and 13, all conditions exhibit cellular-to-cellular dendritic solidification morphologies; increasing laser power enhances melt pool boundary features and pore visibility, while increasing scan speed refines the cellular structure but increases microstructural heterogeneity when remelting becomes marginal.

Mechanistically, the superior appearance and highest relative density measured in the 420 W / 30 mm/s condition arise because the low E_l yields the fastest local cooling rates and steep thermal gradients: Rapid solidification reduces primary arm spacing, suppresses diffusion-controlled precipitation and solute segregation, and shortens the time window for gas entrapment and keyhole instability, producing a uniformly fine austenitic matrix with only very fine, discontinuous carbides or oxides and very few pores; conversely, higher E_l raises melt temperatures and liquid lifetime, coarsens the microstructure, promotes interdendritic segregation and carbide/oxide nucleation, and increases porosity, all of which are evident in the graded progression of OM and SEM features across the nine samples [31].

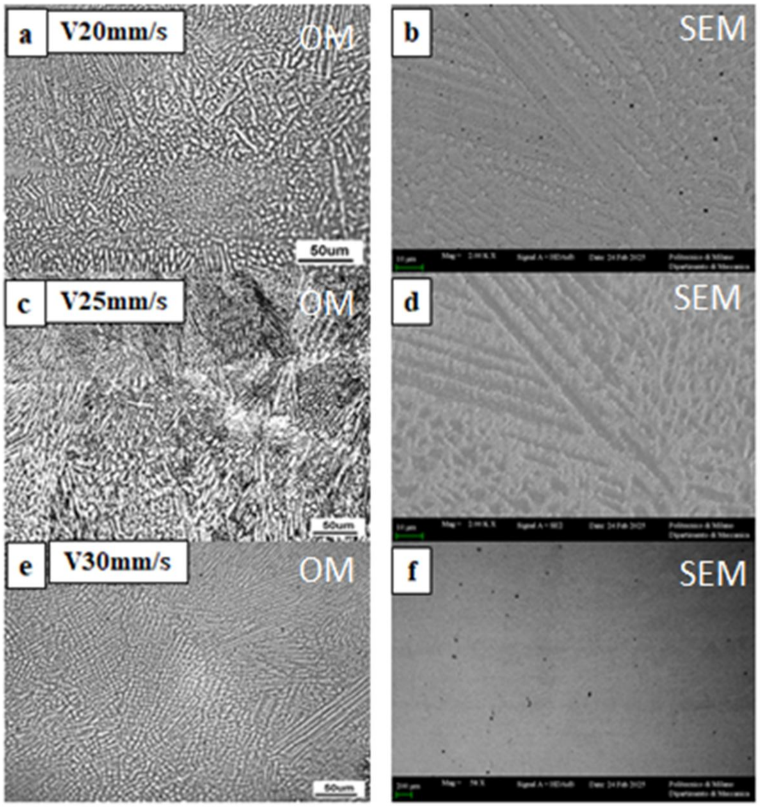

Fig. 13: OM and SEM of SS316L, v of 20, 25, and 30 mm/s at a P of 800 W

3.3. Mechanical Performance through Microhardness Measurement

In this study nine samples of 100% SS316L manufactured by LDED have been examined. The specimens show a very clear, quantitatively strong inverse dependence of Vickers microhardness (as shown in Fig. 14) on the linear energy density across the tested window: samples with the highest E_l (≈40 J/mm at 800 W, 20 mm/s) record the lowest hardness (~185 HV), and those with the lowest E_l (≈14 J/mm at 420 W, 30 mm/s) record the highest hardness (~207 HV). This indication confirms that increasing scan speed (higher v) or reducing power (lower P) raises hardness primarily because both reduce E_l. This behavior is consistent with the laser-AM physics: the cooling rate in the melt/solidification zone scales roughly with scan velocity and inversely with absorbed power (cooling $\propto$ v / P), so higher v or lower P produces faster cooling, finer solidification structures (smaller cellular/dendritic arm spacing or effective grain size), and therefore higher strength/hardness via Hall–Petch–type effects; conversely, high E_l produces larger melt pools, slower cooling, and coarser structures with lower hardness [32, 33]. Directed-energy-deposition (DED) work on AISI 316L shows the same processing physics but also demonstrates that local factors such as lattice micro-strain and subtle phase/δ-ferrite variations can modulate local hardness (so micro-strain/residual stress may either reinforce or partially offset the grain-size effect in specific regions) [34]. Practically, this means that hardness rising as E_l decreases from 40 to 14 J/mm is physically robust and predictable but must be balanced against manufacturing defects: The AM literature also documents that very low energy input (below the material/process-specific threshold) causes unstable melt pools and lack-of-fusion porosity, while overly high energy can produce balling or gas entrapment, so there is an optimal E_l window for good density and the desired mechanical property set [35]. The behavior and quantitative sensitivity fall within published ranges for additively manufactured SS316L and match the theoretical and experimental analyses linking hardness to cooling rate and energy input in laser additive processes.

Any increase in porosity amount (Fig. 15), that is led to decrease in hardness due to localized plastic strain accommodation around voids. Conversely, relative density (which is inversely proportional to porosity as shown in Fig. 16) correlates positively with hardness because a denser material exhibits greater resistance to indentation.

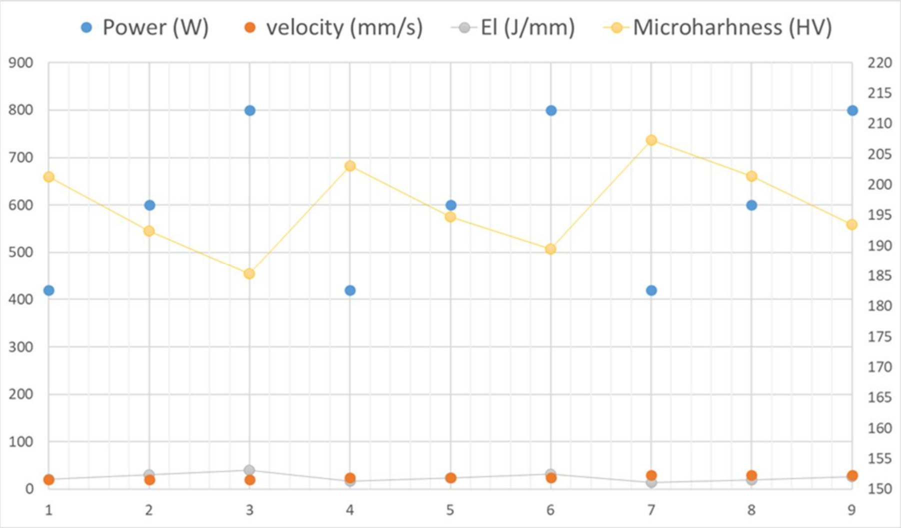

Fig. 14: Relationship between P, ν, E_l, and microhardness.

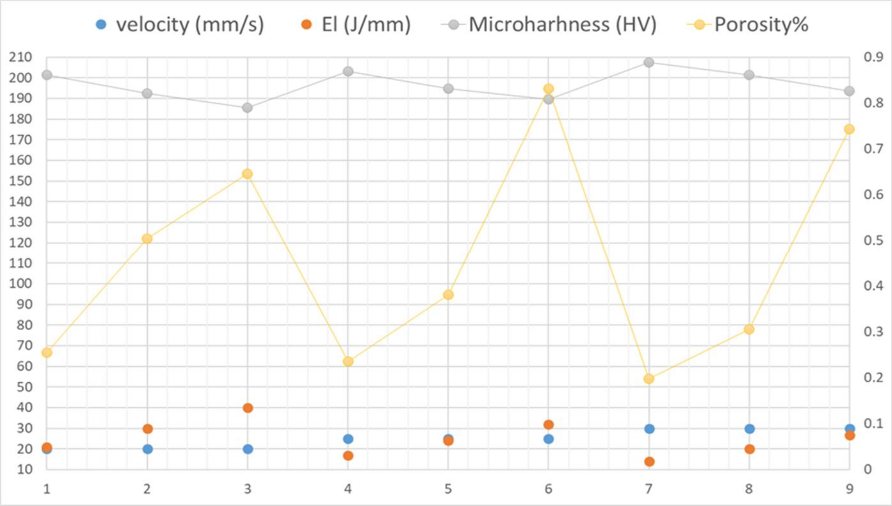

Fig. 15: Relationship between ν, E_l, microhardness, and porosity.

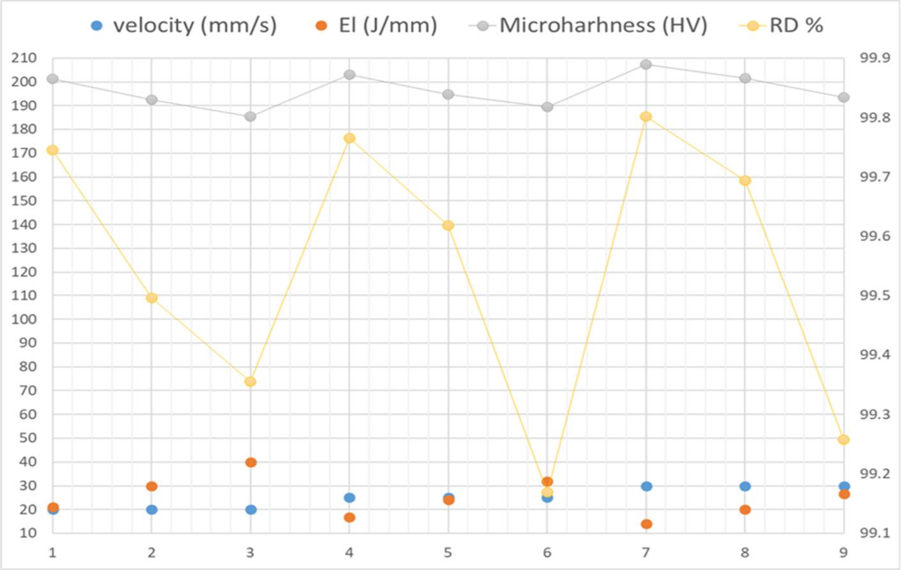

Fig. 16: Relationship between ν, E_l, microhardness, and RD%.

4. Conclusion

This study systematically quantified the effects of laser power and scan speed on porosity formation, relative density, microstructural evolution, and microhardness in SS316L fabricated by laser direct energy deposition.

1- Within the investigated parameter window, porosity ranged from 0.198% to 0.831%, while relative density varied between 99.169% and 99.802%. The lowest porosity (0.198%) and highest relative density (99.802%) were obtained at a scan speed of 30 mm/s and a volumetric energy density of 59 J/mm³, indicating that reduced energy input promotes stable melt pool behavior and effective densification under the present conditions.

2- Optical and scanning electron microscopy revealed that all samples exhibited cellular-to-cellular dendritic austenitic solidification morphologies. Decreasing linear energy density resulted in finer cellular structures, reduced interdendritic segregation, and fewer observable defects, whereas increasing energy density led to coarsened dendritic features, enhanced solute segregation, and a higher incidence of both spherical and irregular pores. These microstructural trends are consistent with variations in melt pool lifetime and local cooling rate induced by changes in laser power and scan speed.

3- Vickers microhardness values ranged from 185.4 to 207.3 HV and showed a clear inverse relationship with linear energy density. Higher scan speeds and lower laser powers produced higher hardness values, which correlate with microstructural refinement associated with faster cooling rates. The measured hardness variations are consistent with grain and cellular spacing refinement rather than changes in phase constitution.

4- Overall, the results demonstrate that laser power and scan speed exert a coupled and quantifiable influence on densification, microstructure, and microhardness in LDED-processed SS316L. The findings define a limited processing window in which porosity is minimized and microstructural refinement is maximized under the fixed conditions employed in this study. These conclusions are restricted to the investigated parameter range and characterization methods and provide an experimental basis for further targeted optimization studies.

Acknowledgment

This work was supported by SITEC-Laboratory for Laser Applications, Department of Mechanical Engineering/ Politecnico di Milano, Italy, with special thanks to Akshay Ashok Benni.

References

[1] S. S. Dash, Z. Liu, L. Lang, T. Lyu, D. Chen, and Y. Zou, “Laser-based direct energy deposition of compositionally graded titanium alloys: Microstructural evolution, hardness, and tensile properties”, J. Alloys and Compounds, 1020, 179335 (2025). doi: 10.1016/j.jallcom.2025.179335

[2] B. Guan, L. Qin, G. Yang, Y. Ren, and X. Wang, “Laser Polishing of Directed Energy Deposition Metal Parts: A Review”, Additive Manufacturing Frontiers, 3, 200174 (2024). doi: 10.1016/j.amf.2024.200174

[3] Y. Chu, X. Zhao, W. Sun, S. Holdsworth, D. Guan, and Y. Huang, “Laser directed energy deposition additive manufacturing using friction stir channelling extruded wire”, Advanced Powder Materials, 2, 100137 (2023). doi: 10.1016/j.jmapro.2025.09.060

[4] T. Zhao, Y. Wang, T. Xu, M. Bakir, W. Cai, M. Wang, M. Dahmen, Q. Zheng, X. Wei, C. Hong, C. Zhong, P. Albus, T. Schopphoven, A. Gasser, and C. L. Häfner, "Some factors affecting porosity in directed energy deposition of AlMgScZr-alloys", Optics & Laser Technology, 143, 107337 (2021). doi: 10.1016/j.optlastec.2021.107337

[5] P. Liu, K. Yi, I. Jeon, and H. Sohn, "Porosity inspection in directed energy deposition additive manufacturing based on transient thermoreflectance measurement", NDT&E International, 122, 102491 (2021). doi: 10.1016/j.ndteint.2021.102491

[6] W. Liu, Y. Li, C. Yao, D. Zhang, D. Sun, S. Chen, Y. Wu, J. Wang, L. Lu, S.-N. Luo, Y. Tao, and B. Zhang, "Revealing mechanism of pore defect formation in laser directed energy deposition of aluminum alloy via in-situ synchrotron X-ray imaging", Condensed Matter Materials Science, 10702 (2024). doi: 10.48550/arXiv.2404.06853

[7] R. Guzmán-Nogales, F. Estupiñán-López, C. Gaona-Tiburcio, O. E. Lopez-Botello, J. G. Ramírez-Rodríguez, and P. C. Zambrano-Robledo, “Corrosion Resistance Measurement of 316L Stainless Steel Manufactured by Selective Laser Melting,” Materials, 14, 4509 (2021). doi: 10.3390/ma14164509

[8] T. E. Abioye, J. Folkes, and A. T. Clare, "A parametric study of Inconel 625 wire laser deposition", J. Materials Processing Technology, 213, 2145-2151 (2013). doi: 10.1016/j.jmatprotec.2013.06.007

[9] N. Ahmed, I. Barsoum, G. Haidemenopoulos, and R. K. Abu Al-Rub, "Process parameter selection and optimization of laser powder bed fusion for 316L stainless steel: A review", J. Manufacturing Processes, 75, 415-434 (2022). doi: 10.1016/j.jmapro.2021.12.064

[10] C. Gianassi, E. Liverani, A. Cavagnino, L. Zarri, A. Ascari, Y. Cui, and A. Fortunato, "Laser directed energy deposition of FeSi/SS 316L advanced bimetallic high-speed rotors: From material characterization to performance evaluation", Advances in Industrial and Manufacturing Engineering, 11, 100175 (2025). doi: 10.1016/j.aime.2025.100175

[11] J. T. Pacheco, V. H. Meura, P. R. A. Bloemer, M. T. Veiga, O. C. de Moura Filho, A. Cunha, and M. F. Teixeira, "Laser directed energy deposition of AISI 316L stainless steel: The effect of build direction on mechanical properties in as-built and heat-treated conditions", Advances in Industrial and Manufacturing Engineering, 4, 100079 (2022). doi: 10.1016/j.aime.2022.100079

[12] Y. Y. Su, Z. F. Wang, J. C. Xie, G. Xu, F. Xing, K. Y. Luo, and J. Z. Lu, "Microstructures and mechanical properties of laser melting deposited Ti6Al4V/316L functional gradient materials", Materials Science & Engineering A, 817, 141355 (2021). doi: 10.1016/j.msea.2021.141355

[13] N. Sargent, Y. Wang, D. Li, Y. Zhao, X. Wang, and W. Xiong, "Exploring Alloy Design Pathway Through Directed Energy Deposition of Powder Mixtures: A Study of Stainless Steel 316L and Inconel 718", Additive Manufacturing Letters, 6, 100133 (2023). doi: 10.1016/j.addlet.2023.100133

[14] A. Saboori, A. Aversa, G. Marchese, S. Biamino, M. Lombardi, and P. Fino, "Microstructure and Mechanical Properties of AISI 316L Produced by Directed Energy Deposition-Based Additive Manufacturing: A Review", Applied Sciences, 10, 3310 (2020). doi: 10.3390/app10093310

[15] G. A. Barragan, F. Mariani, and R. T. Coelho, "Application of 316L stainless steel coating by Directed Energy Deposition process", IOP Conference Series: Materials Science and Engineering, 1154, 012014 (2021). doi: 10.1088/1757-899X/1154/1/012014

[16] H. Shi, T. Wu, Q. Gong, W. Ding, Y. Chai, A. Weisenburger, L. Chang, Z. Zhang, K. Wang, J. Richter, T. Niendorf, and G. Müller, "Hot corrosion behavior of additively manufactured stainless steel 316L and Inconel 718 in MgCl2/KCl/NaCl chloride salts at 700 °C", Corrosion Science, 207, 110561 (2022). doi: 10.1016/j.corsci.2022.110561

[17] Y. Zhou and F. Ning, "Directed Energy Deposition of SS 316L/SiC Composites Using Coincident and Coaxial Wire-Powder Feeding", Procedia Manufacturing, 35, 557-563 (2023). doi: 10.1016/j.mfglet.2023.08.027
[18] Z. Ma, W. Liu, W. Li, H. Liu, Z. Lv, J. Song, Y. Huang, B. Liu, Y. Liu, and Y. Zhang, "Optimization of density and surface morphology of SS 316L/IN718 functionally graded thin-walled structures using hybrid prediction-multi-objective optimization method", J. Manufacturing Processes, 120, 337-352 (2024). doi: 10.1016/j.jmapro.2024.04.044
[19] T. Zurcher, E. Charkaluk, and V. Fridrici, "Wear behavior of 316L stainless steel obtained by additive manufacturing (laser metal deposition process)", Wear, 570, 205948 (2025). doi: 10.1016/j.wear.2025.205948
[20] A. Whitt, R. Seede, J. Ye, M. Elverud, M. Vaughan, A. Elwany, R. Arroyave, and I. Karaman, "A Process Optimization Framework for Laser Direct Energy Deposition: Densification, Microstructure, and Mechanical Properties of an Fe-Cr Alloy", J. Manufacturing Processes, 101, 114 (2022). doi: 10.1016/j.jmapro.2022.11.028
[21] W. Xiong, “Additive manufacturing as a tool for high-throughput experimentation”, J Mater Inf, 2:12 (2022). doi: 10.20517/jmi.2022.19
[22] G. Gong, J. Ye, Y. Chi, Z. Zhao, Z. Wang, G. Xia, X. Du, H. Tian, H. Yu, and C. Chen, "Research status of laser additive manufacturing for metal: a review", J. Materials Research and Technology, 15, 855-884 (2021). doi: 10.1016/j.jmrt.2021.08.050
[23] R. Nagar, R. Singh, N. Patil, and I. Yadav, “Comparison of electrolytic etching and immersion etching for 304L, 316L and 347 austenitic stainless-steel grades”, J. Materials Research and Technology (2024). doi: 10.1515/pm-2024-0032
[24] S. K. Gürel, İ. A. Yüksel, and T. O. Kılınç, “Uncertainty calculations and calibration of metal hardness testing equipment”,19th International Congress of Metrology, 12002 (2019). doi: 10.1051/metrology/201912002
[25] J. Dar, A. G. Ponsot, C. J. Jolma, and D. Lin, "A review on scan strategies in laser-based metal additive manufacturing", J. Materials Research and Technology, 36, 5425-5467 (2025). doi: 10.1016/j.jmrt. (2025).04.068
[26] H. Park, K. M. Mullin, V. Kumar, O. Wander, T. M. Pollock, and Y. Zhu, "Resolving thermal gradients and solidification velocities during laser melting of a refractory alloy", Additive Manufacturing, 105, 104750 (2025). doi: 10.1016/j.addma.2025.104750
[27] G. Liu, Y. Su, X. Pi, D. Liu, and Y. Lin, "Fatigue Strength Improvement of Laser-Directed Energy Deposition 316L Stainless Steel with In Situ Ultrasonic Rolling by Preliminary Investigation", Materials, 17, 3693 (2024). doi: 10.3390/ma17153693
[28] R. Xiao, S. Guo, M. Zheng, D. Zou, and T. Huang, "New method for high-efficiency keyhole-based wire direct energy deposition: Filler wire melting efficiency", Optics & Laser Technology, 193, 114257 (2026). doi: 10.1016/j.optlastec.2025.114257
[29] S. B. Han, Y. Lee, H. Lee, J. S. Jang, S. H. Park, and H. Song, "Tailoring solidification and strength enhancement through process parameter optimization in Nb-added 316L stainless steel fabricated by directed energy deposition (DED)", Journal of Materials Research and Technology, 39, 4532-4543 (2025). doi: 10.1016/j.jmrt.2025.10.082
[30] S. Lee, R. Ghiaasiaan, P. R. Gradl, S. Shao, and N. Shamsaei, "Additively manufactured 316L stainless steel via laser powder directed energy deposition (LP-DED): Mechanical properties at cryogenic and elevated temperatures", International J. Fatigue, 182, 108197 (2024). doi: 10.1016/j.ijfatigue.2024.108197
[31] T. DebRoy, H. L. Wei, J. S. Zuback, T. Mukherjee, J. W. Elmer, J. O. Milewski, A. M. Beese, A. Wilson-Heid, A. De, and W. Zhang, “Additive manufacturing of metallic components – Process, structure and properties”, Progress in Materials Science, 92, 112–224 (2018). doi: 10.1016/j.pmatsci.2017.10.001
[32] Z. Chen, Z. Zhang, Y. Yang, G. Xiao, M. Yi, T. Zhou, and C. Xu, "Influence of interlayer dwell time on microstructure and mechanical properties additively manufactured 316L stainless steel by laser directed energy deposition", J. Materials Research and Technology, 34, 1304-1312 (2025). doi: 10.1016/j.jmrt.2024.12.120
[33] J. Wang, R. Zhu, Y. Liu, and L. Zhang, "Understanding melt pool characteristics in laser powder bed fusion: An overview of single- and multi-track melt pools for process optimization", Advanced Powder Materials, 2, 100137 (2023). doi: 10.1016/j.apmate.(2023).100137
[34] D. Guo, K. Yan, M. D. Callaghan, D. Daisenberger, M. Chatterton, J. Chen, A. Wisbey, and W. Mirihanage, "Solidification microstructure and residual stress correlations in direct energy deposited type 316L stainless steel", Materials & Design, 207, 109782 (2021). doi: 10.1016/j.matdes.2021.109782
[35] P. K. Shanmuganathan, D. B. Purushothaman, and M. Ponnusamy, "Effect of High Laser Energy Density on Selective Laser Melted 316L Stainless Steel: Analysis on Metallurgical and Mechanical Properties and Comparison with Wrought 316L Stainless Steel", 3D Printing and Additive Manufacturing, 10, 3 (2023). doi: 10.1089/3dp.2021.0061

ترسيب الطاقة المباشر بالليزر للفولاذ المقاوم للصدأ 316 L منخفض الكاربون: دراسة تأثير معلمات المعالجة على المسامية وتطور البنية المجهرية

سامر نوري علي[1,*]، زياد أياد طه[1] ، باربارا بريفيتالي[2]

[1]معهد الليزر للدراسات العليا، جامعة بغداد، بغداد، العراق

[2]قسم الهندسة الميكانيكية، بوليتكنيكو دي ميلانو، فيا لا ماسا 1، 20156 ميلانو، إيطاليا

البريد الالكتروني للباحث: *samirnoori@ilps.uobaghdad.edu.iq*

الخلاصة: استخدمت تقنية الترسيب المباشر للطاقة بالليزر (LDED) لتصنيع الفولاذ المقاوم للصدأ منخفض الكربون L316، ولتقييم تأثير معايير المعالجة على المسامية والكثافة النسبية والصلابة المجهرية. استخدم نظام ليزر ليفي يعمل بطول موجي 1070 نانومتر (YLS-3000-CUT، IPG ABB). كان قطر شعاع الليزر 1.2 مم، ومعدل تغذية المسحوق 9.5 غ/دقيقة، وسمك الطبقة 0.2 مم، ومعدل تدفق الغاز الحامل 7.5 لتر/دقيقة، ومعدل تدفق غاز الحماية 25 لتر/دقيقة. تم تغيير قدرة الليزر (420، 600، و800 واط) وسرعة المسح (20، 25، و30 مم/ثانية) بشكل منهجي، مما أنتج تسع عينات بكثافات طاقة خطية تتراوح بين 14 و40 جول/مم^3، وكثافات طاقة حجمية تتراوح بين 59 و167 جول/مم^3. تم فحص الخصائص الميكروية وبنية المسام باستخدام المجهر الضوئي والمجهر الإلكتروني الماسح. وتم تحديد المسامية والكثافة النسبية كميا من خلال تحليل صور المقطع العرضي الكامل. وقيست الصلادة الميكروية باستخدام جهاز فيكرز بحمل 300 غرام وزمن تثبيت 10 ثوان. وتراوحت قيم الصلادة الميكروية بين 185.4 و207.3 HV. وتراوحت قيم المسامية بين 0.198% و0.831%، بينما تراوحت الكثافة النسبية بين 99.169% و99.802%. وأدت كثافات الطاقة الحجمية المنخفضة إلى انخفاض المسامية وزيادة الكثافة النسبية عند جميع سرعات المسح. وتم الحصول على أدنى مسامية (0.198%) وأعلى كثافة نسبية (99.802%) عند سرعة مسح 30 مم/ث وكثافة طاقة حجمية 59 جول/مم^3. تحدد النتائج كميا تأثير قوة الليزر وسرعة المسح على التكثيف والاستجابة الميكانيكية في L316 المعالج بتقنية LDED وتحدد نافذة معالجة محدودة لتقليل العيوب.